Inorganic Chemistry

Article

pubs.acs.org/IC

Field-Induced Spin-Flop in Antiferromagnetic Semiconductors with Commensurate and Incommensurate Magnetic Structures: Li_2FeGeS_4 (LIGS) and Li_2FeSnS_4 (LITS)

Jacilynn A. Brant,[†] Clarina dela Cruz,[‡] Jinlei Yao,[§] Alexios P. Douvalis,[∥] Thomas Bakas,[∥] Monica Sorescu,[⊥] and Jennifer A. Aitken*[,†]

[†]Department of Chemistry and Biochemistry, Duquesne University, Pittsburgh, Pennsylvania 15282, United States

[‡]Quantum Condensed Matter Division, Oak Ridge National Laboratory, Oak Ridge, Tennessee 37381, United States

[§]Research Center for Solid State Physics and Materials, School of Mathematics and Physics, Suzhou University of Science and Technology, Suzhou 215009, China

[∥]Department of Physics, University of Ioannina, Ioannina 45110, Greece

[⊥]Department of Physics, Duquesne University, Pittsburgh, Pennsylvania 15282, United States

Supporting Information

ABSTRACT: Li_2FeGeS_4 (LIGS) and Li_2FeSnS_4 (LITS), which are among the first magnetic semiconductors with the wurtz-kesterite structure, exhibit antiferromagnetism with $T_N \approx 6$ and 4 K, respectively. Both compounds undergo a conventional metamagnetic transition that is accompanied by a hysteresis; a reversible spin-flop transition is dominant. On the basis of constant-wavelength neutron powder diffraction data, we propose that LIGS and LITS exhibit collinear magnetic structures that are commensurate and incommensurate with propagation vectors $\mathbf{k}_m = [^1/_2, ^1/_2, ^1/_2]$ and [0, 0, 0.546(1)], respectively. The two compounds exhibit similar magnetic phase diagrams, as the critical fields are temperature-dependent. The nuclear structures of the bulk powder samples were verified using time-of-flight neutron powder diffraction along with synchrotron X-ray powder diffraction. ^{57}Fe and ^{119}Sn Mössbauer spectroscopy confirmed the presence of Fe^{2+} and Sn^{4+} as well as the number of crystallographically unique positions. LIGS and LITS are semiconductors with indirect and direct bandgaps of 1.42 and 1.86 eV, respectively, according to optical diffuse-reflectance UV−vis−NIR spectroscopy.

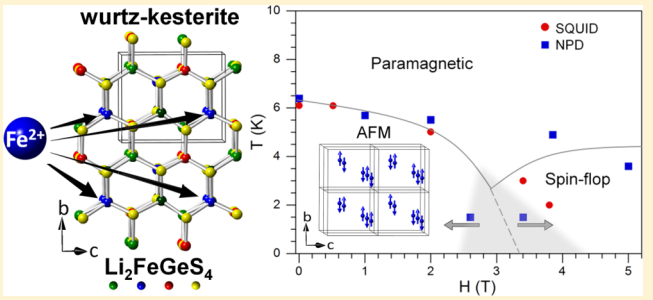

INTRODUCTION

Transition-metal chalcogenides are of interest because of the variety of intriguing crystal structures as well as the valuable properties that can materialize as a result of combining semiconductivity and magnetism. The achievement of room-temperature ferromagnetism in dilute magnetic semiconductors (DMSs) is a current challenge in materials chemistry that, if met, would allow the integration of magnetic and electronic effects for a variety of spintronic applications.[1] Simple diamond structures containing transition metals and chalcogenides provide an avenue for the development of an intimate understanding of the effects of composition and bonding on magnetism as well as other properties. The widely accepted theory is that holes can couple with magnetic ions in these materials to facilitate ferromagnetic interactions. For example, holes can be generated in I−III−VI_2 chalcopyrite-type[2a] diamond-like semiconductors (DLSs) when divalent magnetic ions occupy a portion of the III site.[2b] However, ternary I−III−VI_2[2,3] as well as binary II−VI[4] chalcogenides doped with magnetic ions have not reached the high level of success achieved with binary diamond-like pnictides, such as GaAs:Mn.[5] Obstacles to achieving valuable magnetic properties in chalcogenide DMSs include lack of control in directing magnetic ions to specific lattice sites and solubility limits of the magnetic ion dopants that lead to phase segregation.[1b] In some cases, magnetic ions reside in interstitial sites, clusters, etc., leading to less attractive types of magnetic interactions.

A higher degree of tunability and control can be gained in DLSs as the hierarchy of compositions is extended from binary and ternary to quaternary. In our work, a chalcogenide is employed as the anion in the I_2−II−IV−VI_4 formula. A myriad of cations (e.g., Li, Cu, Ag, Si, Ge, Sn, etc.) can be incorporated to adjust the electronic structure, tuning the bandgap from the UV to the NIR.[6] In these quaternary DLSs, a divalent ion is built into the formula. Therefore, the divalent magnetic ions are easily directed to specific sites within the structure, in contrast to the DLSs obtained through substitutional doping in lower

Received: May 19, 2014

   dx.doi.org/10.1021/ic5011693 | Inorg. Chem. XXXX, XXX, XXX−XXX

tiers of the hierarchy (binary, ternary) (see Figure 1). Magnetic ions are much less likely to occupy interstitial sites and form

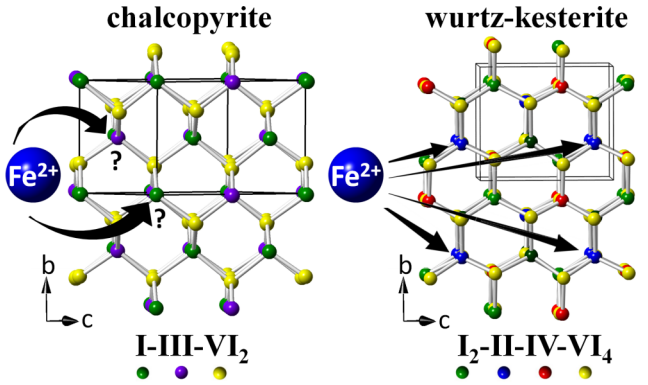

Figure 1. (left) Divalent ions can reside on I- and/or III-sites in the chalcopyrite structure (e.g., $CuInS_2$), whereas (right) divalent ions are directed to specific sites in the wurtz-kesterite structure (e.g., Li_2FeSnS_4).

clusters in I_2–II–IV–VI_4 DLSs than in doped binary and ternary systems. Furthermore, magnetic ions can be incorporated at 12.5 atom % without solubility limit concerns. As a result of these types of simplifications, DLSs with the general formula I_2–II–IV–VI_4 are an attractive platform for tuning electronic structures and magnetic properties, toward the goal of advancing magnetoelectronics.

In fact, the formulae of all diamond-like structures can be calculated, and elements that are capable of exhibiting tetrahedral coordination in conjunction with the appropriate valence can be employed to target DLSs.[7] Since charge balance must be satisfied locally (Pauling's second rule)[8] as well as globally in normal diamond structures, the first coordination sphere of the anion in I_2–II–IV–VI_4 materials consists of two monovalent ions, one divalent ion, and one tetravalent ion. The regular cation ordering, for which there are several options (e.g., stannite, wurtz-stannite, etc.), gives rise to predictable distances between magnetic ions. In contrast to the ∼3.8 Å separation between paramagnetic ions in binary sphalerite/wurtzite DLSs,[9] paramagnetic ions in quaternary DLSs are generally separated by ∼5.5 Å, which can give rise to carrier-mediated magnetic interactions.

Magnetic I_2–II–IV–VI_4 DLSs are usually dominated by antiferromagnetic (AFM) interactions, which have been observed in Cu_2–II–IV–S_4 (II = Mn, Fe; IV = Ge, Sn), Cu_2–II–GeS_4 (II = Co, Ni), and $Cu_2FeSnSe_4$ that crystallize in the stannite and wurtz-stannite structures.[9,10] $Cu_2FeGeSe_4$, with a stannite structure, becomes AFM at 20 K and then undergoes a second transition at ∼8 K to a weak ferromagnetic state.[11] Varying the monovalent ion from Cu to Ag yields $Ag_2FeGeSe_4$ with the wurtz-stannite structure. $Ag_2FeGeSe_4$ is AFM up to 240 K with a very weak superimposed ferromagnetic component due to spin canting, and it shows a larger ferromagnetic contribution below 60 K.[12] Further compositional variations yield ferrimagnetic ordering, which has been reported for $Cu_2FeGeTe_4$,[10e,h] $Ag_2MnSiTe_4$, and $Ag_2MnGeSe_4$.[13] $Cu_2MnSnSe_4$ exhibits spin-glass behavior.[10b] Clearly, compositional changes in diamond-like materials affect the resulting magnetic properties. Interestingly, these magnetic properties can in turn alter the bandgap energies. For example, AFM ordering widens the bandgaps of Cu_2MnGeS_4 and $Cu_2MnSiSe_4$, while ferrimagnetic interactions induce narrower bandgaps in $Ag_2MnGeSe_4$ and $Ag_2MnSiTe_4$.[13] Although there are few examples, $Cu_2Zn_{1-x}Mn_xSnS_4$, $Cu_2Cd_{1-x}Fe_xGeSe_4$, and $Cu_2Cd_{1-x}Mn_xGeSe_4$, which are dominated by AFM interactions, demonstrate that the substitutional doping approach toward DMSs can also be applied to this family.[10h,14] While vast compositions are predicted to possess diamond-like structures, relatively few magnetic DLSs have been explored, and reports of magnetic structures are rare.

Herein, the magnetic and semiconducting properties of Li_2FeGeS_4 (LIGS) and Li_2FeSnS_4 (LITS) are explored. Local and global cation ordering in powder samples of LIGS and LITS are confirmed using synchrotron X-ray powder diffraction (SXRPD), neutron powder diffraction (NPD), and Mössbauer spectroscopy. The bandgaps of LIGS and LITS are assessed using diffuse-reflectance UV–vis–NIR spectroscopy. The magnetic properties are evaluated using a superconducting quantum interference device (SQUID) magnetometer. The magnetic structures of LIGS and LITS, as well as magnetic phase diagrams, are elucidated using NPD measured under an applied field.

EXPERIMENTAL SECTION

Synthesis. All chemicals were used as obtained, unless otherwise noted: (1) lithium sulfide powder (∼200 mesh, 99.9%, Cerac); (2) iron powder (22 mesh, 99.999%, Strem); (3) germanium pieces (99.999%, Strem) were ground into a coarse powder using an impact mortar and pestle and then further ground to a fine powder in a ceramic mortar and pestle; (4) tin powder (∼200 mesh, 99.99%, Cerac); (5) sulfur powder (sublimed, 99.5%, Fisher Scientific).

LITS was prepared by grinding stoichiometric amounts of Li_2S (1 mmol, 0.0460 g), Fe (1 mmol, 0.0559 g), Sn (1 mmol, 0.1187 g), and S (3 mmol, 0.0962 g) using an agate mortar and pestle in an argon-filled glovebox. The reactants were placed into a graphite crucible inside a 12 mm o.d. fused silica tube. The tube was sealed under a pressure of approximately 10^{-3} mbar. The sample was heated at 50 °C/h to 600 °C, held at 600 °C for 96 h, slowly cooled to 350 °C over 50 h, and then allowed to cool to room temperature radiatively. The tube was opened under ambient conditions. LIGS was prepared in a similar manner, but with 20% excess Li_2S to serve as a polychalcogenide flux. The excess Li_2S_x flux was later rinsed with *N*,*N*-dimethylformamide and hexane. Both the LIGS and LITS products are dark-red polycrystalline phases, as observed under an optical microscope. In preparation for all of the physicochemical property measurements, the samples were ground in an agate mortar and pestle for 30 min.

Synchrotron X-ray Powder Diffraction and Rietveld Refinement. High-resolution SXRPD data were collected using beamline 11-BM[15] at the Advanced Photon Source at Argonne National Laboratory using an average wavelength of 0.413046 Å. Discrete detectors covering an angular (2θ) range from −6 to 16° were scanned over a 2θ range of 34°, with data points collected every 0.001° in 2θ at a scan speed of 0.01 deg/s. Rietveld refinements were performed using the General Structure Analysis System (GSAS) with the EXPGUI interface.[16] Details regarding the 11-BM instrument as well as Rietveld refinements can be found in the Supporting Information.

Neutron Powder Diffraction and Rietveld Refinement. Time-of-flight neutron powder diffraction (TOF-NPD) data were collected at the Spallation Neutron Source at Oak Ridge National Laboratory on the POWGEN powder diffractometer. Approximately 4 g of LIGS and ∼2 g of LITS were contained in 8 mm diameter vanadium sample cans. Data for LIGS and LITS were collected using a center wavelength of 1.599 Å, which covers d spacings from 0.5519 to 4.1207 Å. The Fast Exchange Refrigerator for Neutron Scattering was used to collect data for LIGS at 20 and 300 K and data for LITS at 15, 50, and 300 K. The data collected at POWGEN, which offers good resolution at high Q ($\Delta d/d$ = 0.0015 at d = 1 Å)[17] that can allow

dx.doi.org/10.1021/ic5011693 | Inorg. Chem. XXXX, XXX, XXX–XXX

refinement of U_{iso} values and nuclear structure verification, complement NPD data collected at the High Flux Isotope Reactor on the HB-2A diffractometer at Oak Ridge National Laboratory.

Constant-wavelength neutron powder diffraction (CW-NPD) data were collected at HB-2A with a wavelength of 2.4063 Å. The minimum peak full width at half-maximum was 0.2°. HB-2A has capabilities for data collection at low temperatures (e.g., 2 K) under applied magnetic fields while providing the high intensity at low Q that was vital in assessing the magnetic structures and phases of the LIGS and LITS systems. The full powder patterns were collected at 20 and 1.5 K in the absence of an applied field and with applied magnetic fields up to 5 T. Also, the intensities of magnetic peaks were followed as functions of both temperature and applied magnetic field to assess the boundaries for magnetic phase transitions.

Rietveld refinements using CW-NPD data were conducted using FullProf.[18] Peaks arising from magnetic interactions were indexed using the k-search function in FullProf. Additional details regarding the POWGEN and HB-2A instruments as well as Rietveld refinements can be found in the Supporting Information.

^{57}Fe and ^{119}Sn Mössbauer Spectroscopy. ^{57}Fe and ^{119}Sn Mössbauer spectra were collected on ground powder samples using constant-acceleration spectrometers equipped with ^{57}Co(Rh) and Ca^{119m}SnO$_3$ sources kept at room temperature (RT = 300 K). Two liquid N_2 variable-temperature cryostats (Oxford Instruments Variox 316 and Thor Cryogenics) were used for the measurements at 77 K (^{57}Fe resonance) and 80 K (^{119}Sn resonance). The spectrometers were calibrated with metallic α-Fe at RT. Analyses of the spectra were performed with sets of paramagnetic doublets, assuming Lorentzian line shapes, using a recently developed Mössbauer fitting program.[19] The isomer shift (δ) values of the components used to fit the spectra are given relative to α-Fe at 300 K for the ^{57}Fe spectra and relative to SnO_2 at 300 K for the ^{119}Sn spectrum. Parameters obtained from data fitting are displayed in Tables S9 and S10 in the Supporting Information.

Optical Diffuse-Reflectance UV−Vis−NIR Spectroscopy. Optical diffuse-reflectance spectra were collected using a Cary 5000 UV−vis−NIR spectrometer. $BaSO_4$ (99.92%, Fisher Scientific) was used as a 100% reflectance standard. The LIGS and LITS samples were ground and placed into a sample cup in a Harrick Praying Mantis diffuse-reflectance accessory, and scans were performed from 200 to 2500 nm at a rate of 600 nm/min. The percent reflectance data were converted to absorption using the Kubelka−Munk equation,[20] and wavelength was converted to energy. To estimate the Urbach energy, the data were fit using eq 1,

$$f(E) = A \exp[(E - E_g)/E_u] \quad (1)$$

in which A is a constant, E_g is the bandgap, and E_u is the Urbach energy.[21]

Magnetic Measurements. Magnetization data in zero-field-cooled mode for the polycrystalline powder samples were measured on a Quantum Design SQUID magnetometer over the temperature range of 2−300 K. Measurements were carried out in applied fields of 0.5, 2, and 5 T over the temperature range of 2−20 K. The isothermal field dependence of the magnetization was measured with the magnetic field varying between 0 and 5 T. Corrections for intrinsic diamagnetism were applied to all of the data.[22] The data were fit to a modified Curie−Weiss law, and details are provided in section S6 in the Supporting Information.

RESULTS AND DISCUSSION

Structure. LIGS and LITS can be considered as the lithium analogues of the minerals briartite (Cu_2FeGeS_4)[23] and stannite (Cu_2FeSnS_4).[24] However, the structures of briartite and stannite crystallize in the space group $I\bar{4}2m$ and are structurally derived from cubic diamond, whereas the title compounds are structural derivatives of lonsdaleite, the rare hexagonal diamond.[25] Both LIGS and LITS crystallize in the space group Pn[26a] with structures related to wurtz-kesterite,[26b,c] as previously reported.

The structures of LIGS and LITS comprise a hexagonal closest packed array of S^{2-} anions wherein Li^+, Fe^{2+}, and Sn^{4+} or Ge^{4+} occupy half of the tetrahedral holes (see Figure 1, right).[26a] The structure consists of two crystallographically independent Li sites, one Fe site, one Sn or Ge site, and four S sites, all residing on general positions. As expected, the electrostatic valence principle is satisfied, as each sulfide anion is coordinated by one Fe^{2+}, one Sn^{4+} or Ge^{4+}, and two Li^+ ions. The crystal structures of LIGS and LITS have been solved and refined with R_1 (all data) = 0.0346 and 0.0310, respectively.[26a] In the otherwise satisfactory crystal structures, the atomic displacement parameters (ADPs) of the lithium ions were physically unreasonable. Lithium sites were refined isotropically with U_{iso} values of 0.004(3) and 0.103(1) Å^2 for LITS and 0.007(3) and 0.024(5) Å^2 for LIGS. These types of irregular displacement parameters are commonly observed for light elements such as lithium and are due to small X-ray scattering factors; thus, neutron diffraction (Figure 2) was employed to verify the positions, ADPs, and site occupation factors (SOFs) of the lithium sites.

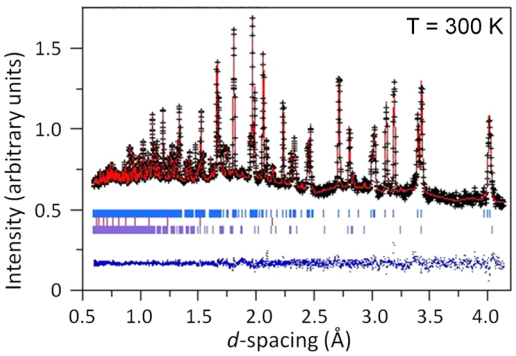

Figure 2. Results of Rietveld refinement for Li_2FeSnS_4. The collected time-of-flight neutron powder diffraction data are plotted with plus signs (+), overlapped with the pattern calculated using the model (line). The expected Bragg reflections for Li_2FeSnS_4, vanadium (from the sample can), and SnS are displayed from top to bottom with tick marks (|). The difference between the collected data and the calculated pattern is shown at the bottom of the plot.

Rietveld refinements of the LIGS and LITS structures were carried out using TOF-NPD data that were collected at 300 K. While the resulting structure models were in good agreement with those obtained using X-ray diffraction data, the ADPs refined to reasonable values. In the LIGS structure, the U_{iso} values of Li(1) and Li(2) refined to 0.018(4) and 0.025(6) Å^2, respectively. Finally, free refinement of the SOFs of the Li sites using the TOF-NPD data indicated that the Li sites are fully occupied (Li(1) SOF = 0.99(3) and Li(2) SOF = 0.99(5)). In the LITS structure, the U_{iso} values of Li(1) and Li(2) refined to 0.010(2) and 0.014(2) Å^2, respectively. Freely refining the SOFs yielded values of 0.99(3) for Li(1) and 1.01(3) for Li(2). These results confirm that the lithium sites are fully occupied, as would be expected in a wurtz-kesterite structure that exhibits cation ordering.

Ordered cations are generally observed in this family of quaternary I_2−II−IV−VI_4 DLSs, with some exceptions.[27] For example, the Cu_{Zn} and Zn_{Cu} antisite defects that are prevalent in Cu_2ZnSnS_4 (CZTS) and $Cu_2ZnSnSe_4$ (CZTSe),[28] especially samples that undergo rapid quenching, likely arise because Cu^+

dx.doi.org/10.1021/ic5011693 | Inorg. Chem. XXXX, XXX, XXX−XXX

and Zn^{2+} are isoelectronic and have identical crystal radii.[29] While the tetrahedral cations in LITS and LIGS are not isoelectronic and have disparate ion sizes (Li^+, 0.73 Å; Fe^{2+}, 0.77 Å; Ge^{4+}, 0.53 Å; Sn^{4+}, 0.69 Å),[29] it is worthwhile to verify the coordination sphere and resulting cation ordering since it dictates the nature of the magnetic interactions. Furthermore, noncompliance with Pauling's second rule could introduce superexchange (Fe−S−Fe) interactions.

Mössbauer Spectroscopy. ^{57}Fe Mössbauer spectroscopy was used to further confirm the structures of LIGS and LITS as well as the presence or absence of any Fe-containing impurities that could have significant effects on the magnetic measurements. The ^{57}Fe Mössbauer spectra of the LIGS sample exhibit a pronounced dominant doublet with isomer shift (δ) values of 0.66 and 0.77 mm/s at 300 and 77 K, respectively (Figure 3 and Table S9 in the Supporting Information).

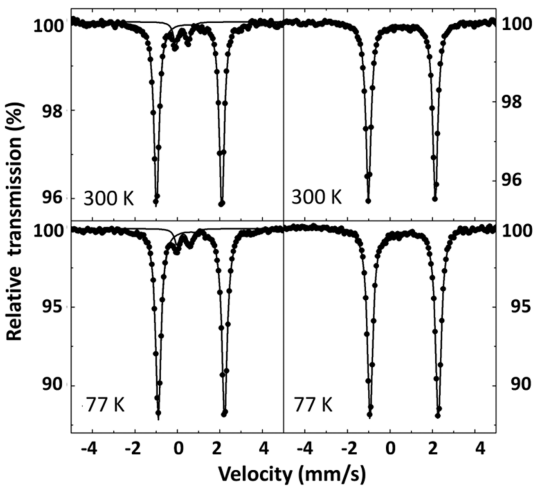

Figure 3. ^{57}Fe Mössbauer spectra of (left) Li_2FeGeS_4 and (right) Li_2FeSnS_4 collected at 300 and 77 K.

In the closely related Cu_2FeSnS_4, Fe^{2+} ions that compose the FeS_4 tetrahedra give rise to δ values of 0.57−0.62 mm/s.[30] Similarly, tetrahedral Fe^{2+} in $Cu_{10}Fe_2Sb_4S_{13}$, $FeCr_2S_4$, and zinc blende-type (Fe,Zn)S yields δ values of 0.61, 0.60, and 0.66 mm/s, respectively.[31] In contrast, Fe^{3+} ions that occupy FeS_4 tetrahedra in $CuFeS_2$ were assigned to lower δ values of 0.20−0.40 mm/s.[30d,32] The δ values for tetrahedral Fe^{3+} in other sulfides such as $CuIn_{1-x}Fe_xS_2$, Cu_5FeS_4, $Cu_3(Ge,Fe)S_4$, $TlFeS_2$, and $Cu_{12}Fe_{0.5}Sn_4S_{13}$ range from 0.18 to 0.51 mm/s.[30d,31,33] Furthermore, increasing coordination number yields higher δ values. In phosphate minerals, distorted bipyramidal Fe^{2+} gives rise to δ values of 1.10−1.16 mm/s,[34] and octahedral Fe^{2+} ions have been assigned to δ values of 1.15−1.27 mm/s.[35] Thus, the δ values detected for the dominant doublet of the LIGS sample spectra are characteristic of Fe^{2+} states in a sulfur-coordinated tetrahedral environment. The minor doublet, which is characteristic of Fe^{3+}, comprises ∼7−9% of the absorption area of the ^{57}Fe Mössbauer spectra of the LIGS sample and can be attributed to some unavoidable partial oxidation of the surface of the sample. Indeed, it was noted that samples of LIGS left out on the bench for a few months noticeably changed color as a result of oxidation, whereas the LITS sample seemed to be less susceptible to oxidation.

As evidenced from Figure 3, clearly only one doublet needed to be included in the model for the ^{57}Fe Mössbauer spectra of the LITS sample. The resulting δ values of 0.67 and 0.78 mm/s at 300 and 77 K, respectively (Table S9), denote Fe^{2+} states in a sulfur-coordinated tetrahedral environment for the iron ions in the LITS sample as well, with an absence of Fe^{3+} impurities.

An even more telltale sign of ferrous tetrahedra lies in the quadrupole splitting (ΔE_Q) values. The Fe^{2+} states in the spectra of LIGS and LITS exhibit ΔE_Q values of 3.07 and 3.15 mm/s, respectively, at 300 K, which are slightly higher at 77 K (see Table S9). Fe^{2+}-containing tetrahedra in Cu_2FeSnS_4 yield ΔE_Q values of 2.89−2.92 mm/s.[30] Similarly, tetrahedral Fe^{2+} ions in $Cu_{10}Fe_2Sb_4S_{13}$ are correlated with a ΔE_Q value of 2.90 mm/s.[31] Greater distortion within the FeS_4 tetrahedron gives rise to larger ΔE_Q.[30a] Accordingly, the relatively large ΔE_Q values of the title compounds are attributed to the distortion introduced into the FeS_4 tetrahedra by incorporation of lithium into the coordination sphere of sulfur.

In our measurements, the narrow peak half-widths ($\Gamma/2$ = 0.14−0.16 mm/s; see Table S9) indicate that the Fe^{2+} resides in one crystallographically unique position, which is in agreement with our structure determined from X-ray diffraction. The results of ^{57}Fe Mössbauer spectroscopy for diamond-like Cu_2FeSnS_4 and $CuFeS_2$ were also in agreement with X-ray diffraction results, indicating ordered structures.[30a,32]

The ^{119}Sn Mössbauer data are in agreement with the ordered arrangement of Sn^{4+} cations in LITS. The ^{119}Sn Mössbauer spectrum contains a pronounced main doublet with δ = 1.28 mm/s and ΔE_Q = 0.28 mm/s (Figure 4 and Table S10 in the Supporting Information) that corresponds to one crystallographically unique Sn^{4+}. This result is in close proximity to the single broad absorption peak (a macroscopically unresolved doublet) in the range of 1.45−1.48 mm/s observed for tetravalent tin in SnS_4 tetrahedra within stannite.[30a,b,e] Sn^{4+} ions in SnS_4 tetrahedra in the ternary tin sulfides Na_4SnS_4, Ba_2SnS_4, $Na_6Sn_2S_7$, $Ba_3Sn_2S_7$, and Tl_2SnS_3 give rise to δ values ranging from 1.17 to 1.23 mm/s.[36] In contrast to our results, octahedral Sn^{4+} ions in Sn_2S_3 and SnS_2 yield δ values of 1.09−1.19 mm/s[37] and 1.01−1.06 mm/s,[37a,38] respectively. Furthermore, the tetrahedral coordination of Sn in our LITS was clearly discerned using X-ray diffraction.

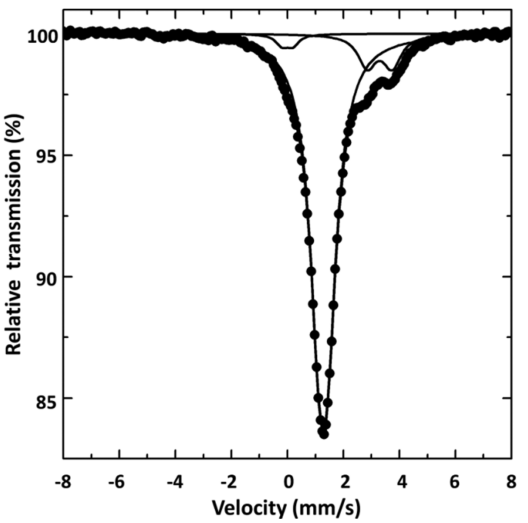

Figure 4. ^{119}Sn Mössbauer spectrum of Li_2FeSnS_4 collected at 80 K.

Divalent tin is assigned much higher δ values. Sn^{2+} with octahedral, bicapped trigonal prismatic, and square-based pyramidal geometries in $SnBi_2Te_4$, $GeSnS_3$, and $In_2Sn_3S_7$

dx.doi.org/10.1021/ic5011693 | Inorg. Chem. XXXX, XXX, XXX−XXX

exhibit δ values of 3.3, 3.50, and 3.82 mm/s, respectively.[37b,39] The δ values are reported to appear at 3.16−3.60 mm/s for Sn^{2+} with three nearest neighbors in SnS and Sn_2S_3.[37a,b,40] In our spectrum, the two low-intensity doublets with δ values of 3.29 and 0.00 mm/s and ΔE_Q values of 0.90 and 0.38 mm/s are attributed to Sn^{2+} and Sn^{4+} ions in SnS and SnO_2 impurities, respectively.[41,42] These results are in agreement with the minor SnS impurity modeled in our Rietveld refinements using SXRPD and NPD data, while the minor SnO_2 impurity detected by ^{119}Sn Mössbauer spectroscopy was not detected by diffraction methods.

Synchrotron X-ray Powder Diffraction. Different patterns of cation arrangements are possible in multication diamond-like structures such as stannite ($I\bar{4}2m$) and kesterite ($I\bar{4}$), which are structural derivatives of cubic diamond, as well as lithium cobalt(II) silicate ($Pna2_1$), wurtz-stannite ($Pmn2_1$), and wurtz-kesterite (Pn), which are structural derivatives of hexagonal diamond. These variations in global cation ordering in I_2−II−IV−VI_4 DLSs can result from compositional changes but have also been observed within a single composition (e.g., α- and β-Cu_2ZnSiS_4 with wurtz-stannite and wurtz-kesterite structures).[6c] While the differences in the powder diffraction patterns resulting from these polymorphs may be difficult to discern using laboratory X-ray powder diffraction, they can be revealed using high-resolution SXRPD. As these types of structural variations can affect the magnetic interactions, it is important to critically assess the structure of the bulk microcrystalline powder on which the magnetic studies are conducted.

According to SXRPD, the LIGS and LITS powder samples have the wurtz-kesterite structure. Rietveld refinement of LITS (Figure 5), with χ^2 = 1.970, R_p = 0.0825, and wR_p = 0.1001,

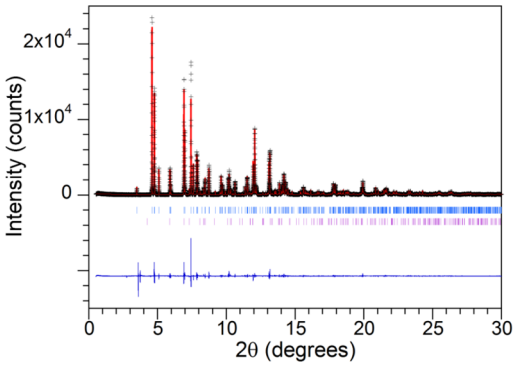

Figure 5. Results of Rietveld refinement for Li_2FeSnS_4. The collected synchrotron X-ray powder diffraction data are plotted with plus signs (+), overlapped with the pattern calculated using the model (line). Data up to 2θ = 30° are shown, while data for higher angles up to 2θ = 50° were included for the refinement. The expected Bragg reflections for the Li_2FeSnS_4 and SnS are displayed from top to bottom with tick marks (|). The difference between the collected data and the calculated pattern is shown at the bottom of the plot.

supports the presence of a minor (4.86 wt %) SnS impurity phase,[42] which corresponds to the Sn^{2+} observed in the Mössbauer spectrum. According to Rietveld refinement of LIGS (Figure S1 in the Supporting Information), this sample also has high phase purity. However, a small number of extra peaks with low intensity were indexed to a hexagonal phase in the space group $P6_3mc$ and modeled using the LeBail method within GSAS/EXPGUI. Agreement factors of χ^2 = 4.059, R_p = 0.1184, and wR_p = 0.1563 were achieved. In both LIGS and LITS, the impurities are very minute, and neither impurity phase was detectable with laboratory-grade X-ray powder diffraction. These minor secondary phases are more easily revealed using SXRPD because of the brighter source. The models of both LIGS and LITS are in good agreement with those refined using TOF-NPD data and further support the high degrees of order and phase purity.

Diffuse-Reflectance Spectroscopy. Optical bandgaps of LIGS and LITS were estimated using diffuse-reflectance UV−vis−NIR spectroscopy (Figure 6). Urbach tailing is observed near the absorption edge and corresponds to a broadened distribution of electronic states around the bandgap.[21b] The Urbach tail region, which extends up to 2.05 eV for LIGS and 1.98 eV for LITS according to the fit to eq 1, was negated for determination of the bandgap. When the data are rescaled to emphasize direct and indirect optical transitions,[21b,43] direct transitions are signified by a wider region of linearity in the plot of $(\alpha E)^2$ versus E, while indirect transitions correspond to wider linearity in the plot of $(\alpha E)^{1/2}$ versus E. These regions of linearity were assessed at energies above the Urbach tail region. Accordingly, LIGS is an indirect-gap semiconductor, and the data were fit using eq 2,

$$\alpha(E) = A(E - E_g)^2/E \quad (2)$$

yielding a bandgap of 1.423(3) eV. This bandgap, which corresponds to a wavelength of 874 nm at the border of the visible and near-infrared regions of the electromagnetic spectrum, is in agreement with the dark-red color of polycrystalline LIGS. LITS is a direct-gap semiconductor. Fitting the data using eq 3,

$$\alpha(E) = A(E - E_g)^{1/2}/E \quad (3)$$

yielded a bandgap of 1.860(2) eV (667 nm), which is in agreement with the red color of LITS. Simply altering the IV ions used for the synthesis of Li_2Fe−IV−S_4 DLSs changes the nature of the bandgap. Just as in the wurtz-stannite Li_2CdGeS_4 and Li_2CdSnS_4 DLSs,[6d,e] the germanium-containing compound exhibits a narrower bandgap than the tin analogue, although the opposite trend is often observed.[44a] The bandgaps in these materials can be potentially tuned for optimal photovoltaic performance.[44]

Magnetic Properties. According to magnetization measurements, LIGS and LITS are AFM below the Néel temperatures (T_N) of ∼6 and ∼4 K, respectively. The magnetizations were measured as functions of temperature, and the Néel temperatures were taken as the inflection points of the curves shown on the left in Figure 7. The magnetization data measured under an applied field of 0.5 T were equivalent to those measured under zero-field-cooled conditions. The magnetization was also measured under constant applied fields of 2 and 5 T. In both LIGS and LITS, T_N decreases with increasing applied field and could not be determined at an applied field of 5 T at temperatures down to 2 K.

The magnetization was also measured as a function of applied field at constant temperatures, as shown on the right in Figure 7. Both compounds undergo a conventional metamagnetic transition accompanied by hysteresis, which is typical for a reversible spin-flop transition.[45] The critical field (H_c) for the spin-flop transition, which is taken as the onset of the hysteresis, is approximately 3 T for LIGS and 2 T for LITS at 2 K.

dx.doi.org/10.1021/ic5011693 | Inorg. Chem. XXXX, XXX, XXX−XXX

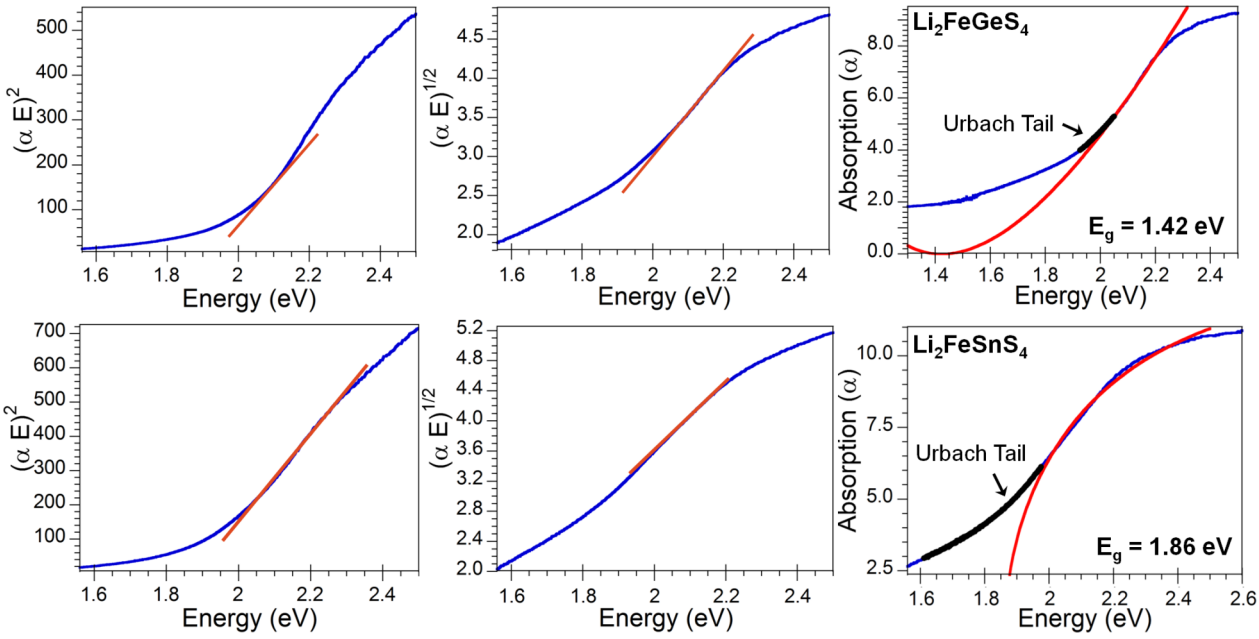

Figure 6. Diffuse reflectance UV−vis−NIR spectra for (top) Li_2FeGeS_4 and (bottom) Li_2FeSnS_4, rescaled to emphasize (left) direct and (center) indirect optical transitions. The data for Li_2FeGeS_4 were fit using Tauc's function[43] for indirect-gap semiconductors, while the Urbach tail region was excluded from the absorption edge (top right). The data for Li_2FeSnS_4 were fit using Tauc's function for direct-gap semiconductors (bottom right).

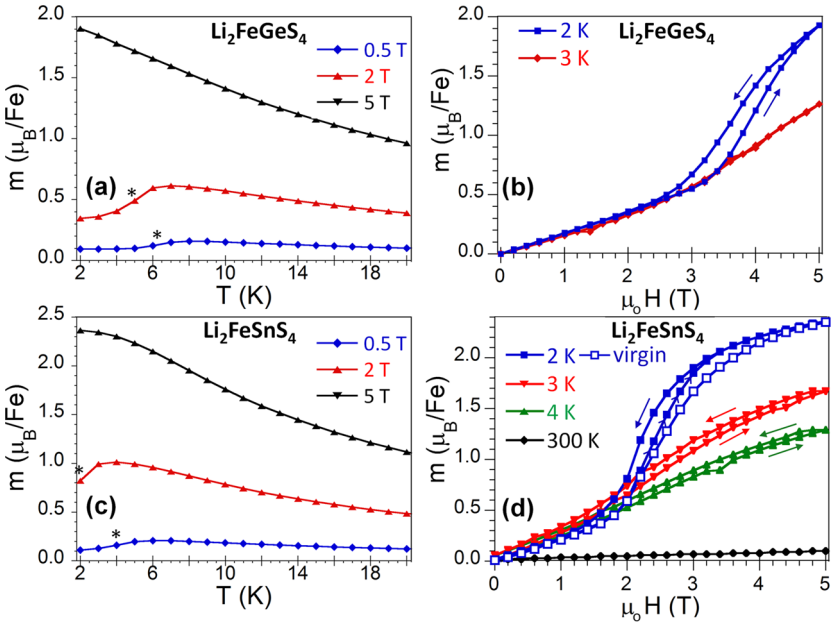

Figure 7. (a, c) Temperature dependence of the magnetization collected at constant applied fields. Néel temperatures were assigned as the inflection points (*). (b, d) Field dependence of the magnetization collected at constant temperatures.

Antiferromagnetism similar to that observed in LIGS and LITS has been observed among magnetic I_2−II−IV−VI_4 DLSs. For example, AFM Cu_2FeSnS_4 has T_N = 6.1 K,[9] and the transition temperature can be modified to $T_N \approx 12$ K by employing Ge as the IV ion in Cu_2FeGeS_4[10g] or to $T_N \approx 19$ K by using Se as the VI ion in $Cu_2FeSnSe_4$.[10b] Similarly, $Cu_2FeGeSe_4$ is also AFM with T_N = 20 K.[10e] Although a handful of magnetic I_2−II−IV−VI_4 phases have been studied, these works have rarely reported the magnetic structures.[10d,g,23]

Magnetic Structure. Since magnetic structures of I_2−II−IV−VI_4 DLSs are scarce, we decided to elucidate the magnetic structures of AFM LIGS and LITS using CW-NPD. Structure models that resulted from Rietveld refinements using CW-NPD data collected at temperatures above T_N were in good agreement with the nuclear structures modeled using TOF-NPD data collected at the same temperatures (Tables 1 and 2). Atomic coordinates, atomic displacement parameters, and bond distances are available in Tables S1−S8 in the Supporting Information. Upon cooling below T_N, extra peaks that can be attributed to magnetic ordering were observed in the NPD patterns of both LIGS and LITS, while the intensities of peaks corresponding to the nuclear structure did not change at lower temperature.

dx.doi.org/10.1021/ic5011693 | Inorg. Chem. XXXX, XXX, XXX−XXX

Table 1. Results from Rietveld Refinements of Neutron Powder Diffraction Data for Li_2FeGeS_4 (TOF = Time of Flight; CW = Constant Wavelength)

	TOF		CW		
	300 K	20 K	20 K	0 T, 1.5 K	3.8 T, 1.5 K
a (Å)	6.2294(1)	6.2238(1)	6.2235(6)	6.2227(3)	6.2224(3)
b (Å)	6.6107(1)	6.6036(1)	6.6017(6)	6.6025(3)	6.6018(3)
c (Å)	7.8081(2)	7.7859(2)	7.7821(7)	7.7825(3)	7.7820(3)
β (deg)	90.311(2)	90.328(2)	90.333(6)	90.334(4)	90.330(3)
V (Å^3)	321.55(1)	319.993(8)	319.72(5)	319.74(2)	319.67(2)
χ^2	5.086	5.643	3.53	3.37	3.30
R_p	0.0547	0.0591	0.0794	0.0809	0.0758
wR_p	0.0238	0.0270	0.102	0.103	0.101

Table 2. Results from Rietveld Refinements of Neutron Powder Diffraction Data for Li_2FeSnS_4 (TOF = Time of Flight; CW = Constant Wavelength)

	TOF		CW		
	300 K	50 K	50 K	0 T, 1.5 K	2.5 T, 1.5 K
a (Å)	6.37419(7)	6.373(2)	6.3654(9)	6.3732(3)	6.3732(3)
b (Å)	6.78396(7)	6.7814(2)	6.776(1)	6.7779(3)	6.7780(3)
c (Å)	7.93071(9)	7.9183(3)	7.918(1)	7.9168(4)	7.9165(4)
β (deg)	90.2639(9)	90.279(3)	90.27(2)	90.282(5)	90.279(5)
V (Å^3)	342.938(5)	342.21(2)	341.51(9)	341.98(3)	341.97(3)
χ^2	1.303	1.807	1.35	1.52	1.84
R_p	0.0102	0.0667	0.0787	0.0540	0.0589
wR_p	0.0171	0.1070	0.101	0.0678	0.0769

For LIGS, the additional peaks were indexed to a magnetic structure with a propagation vector $\mathbf{k}_m = [^1/_2, ^1/_2, ^1/_2]$, which indicates that the magnetic structure is commensurate with the nuclear structure (see Figure 8). The magnetic moments were constrained to be collinear. Combining the nuclear and magnetic structure models in the Rietveld refinement resulted in a χ^2 of 3.37, and the fit of the magnetic peaks lies within experimental error, as shown with the solid line in the Figure 8a inset. The magnetic moment refined to 2.82(7) μ_B/Fe along the b axis, which is lower than the expected saturated magnetic moment for the high-spin tetrahedral Fe^{2+} free ion ($S = 2$; $\mu_{sat} = 4\ \mu_B$) and the value of 3.76 μ_B/Fe obtained by fitting the Curie–Weiss law to the data at $T > 125$ K (Section S6 in the Supporting Information). It is also lower than the observed magnetic moments that have been reported for Cu_2FeGeS_4 and Cu_2FeSnS_4 (4.7–5.01 μ_B).[10g,46]

Similar to LIGS, Cu_2MnSnS_4 exhibits collinear magnetic ordering, as determined using single-crystal neutron diffraction.[10d] The magnetic structure of stannite-type Cu_2MnSnS_4 is described with a propagation vector $\mathbf{k}_m = [^1/_2, 0, ^1/_2]$. Similar to the commensurate magnetic structure of LIGS, the magnetic unit cell of Cu_2MnSnS_4 doubles along the a and c axes, while the magnetic unit cell of LIGS also doubles along the b axis. In contrast, the magnetic moments of Cu_2MnSnS_4 are oriented 16° from the c axis. The NPD peaks arising from magnetic ordering of LIGS are indexed to $h0l$. Thus, the magnetic moments are aligned along the b axis since intensity contributions are provided only to the scattering plane that is perpendicular to the moment.

The highest-intensity peak associated with magnetic ordering in LIGS was observed at 0.82 Å^{-1}, and the intensity was followed both as a function of temperature and as a function of applied magnetic field to establish phase boundaries of the paramagnetic, AFM, and field-induced phases (Figure 9). When the peak intensity was followed with varying temperature under zero field, the onset of magnetic ordering (T_N) was ~6.4 K (Figure 8c). The intensity of the peak at 0.82 Å^{-1} decreased under an applied field of 3.8 T ($H > H_c$). The magnetic structure of the spin-flop phase was difficult to confirm because of the small number of relatively low intensity magnetic peaks. When the simple AFM model with $\mathbf{k}_m = [^1/_2, ^1/_2, ^1/_2]$ was considered, the magnetic moments refined to 1.86(9) μ_B/Fe.

Furthermore, evidence of remanent magnetization was not observed. The metamagnetic phase was approached from (1) high temperature (20 K) at a constant applied field of 3.8 T, (2) zero field at a constant temperature of 1.5 K, and (3) high field (5 T) at a constant temperature of 1.5 K. Minimal variations in the intensities of the peaks associated with magnetic ordering were observed. However, the Néel temperature obtained by following the 0.82 Å^{-1} peak intensity with increasing applied field (0 to 5 T) at a constant temperature of 1.5 K was different than that obtained when the same measurement was conducted with a decreasing applied field (5 to 0 T). The critical fields (H_c) of ~3.4 and ~2.6 T, respectively, are shown with arrows in the magnetic phase diagram (Figure 9).

Similar to the case of LIGS, the nuclear structures of LITS at 300, 50, and 1.5 K were in good agreement (Table 2). Magnetic ordering was evident in the CW-NPD pattern collected at 1.5 K, with the largest magnetic peak appearing at 0.43 Å^{-1} (Figure 10). The magnetic ordering in LITS can be indexed with a propagation vector $\mathbf{k}_m = [0, 0, 0.546(1)]$, indicating an incommensurate AFM structure. When the magnetic moments were constrained to be collinear, the moments refined to 3.6(2) μ_B/Fe, which is close to the value of 3.92 μ_B/Fe obtained by fitting the magnetization data at $T > 10$ K with a modified Curie–Weiss law (Section S6 in the Supporting Information). While these moments are larger than those in LIGS, they are still lower than expected. As the d electrons in iron participate in covalent bonding with sulfur, it is reasonable that the

dx.doi.org/10.1021/ic5011693 | Inorg. Chem. XXXX, XXX, XXX–XXX

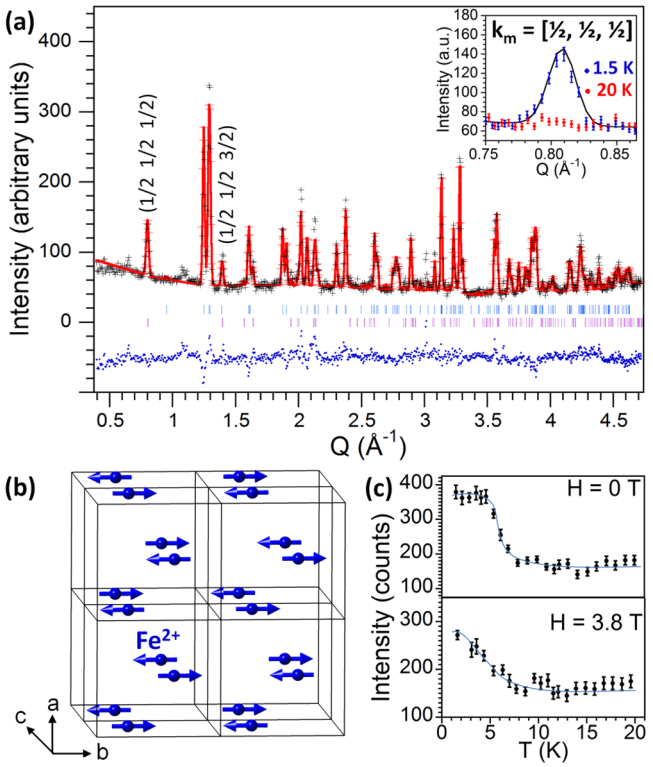

Figure 8. (a) Rietveld refinement of constant-wavelength neutron powder diffraction data for Li_2FeGeS_4 collected at 1.5 K. Indices for main peaks from the magnetic structure are labeled. Bragg reflections for the nuclear and magnetic structures are displayed from top to bottom (|). The difference between the collected data (+) and the calculated pattern (line) is shown at the bottom of the plot. The inset shows a peak attributed to magnetic ordering, and the fit of the magnetic structure is shown with a line. (b) Magnetic unit cell of Li_2FeGeS_4. (c) Temperature dependence of the intensities of the magnetic peak at 0.82 Å^{-1}. Lines provide guides for the eye.

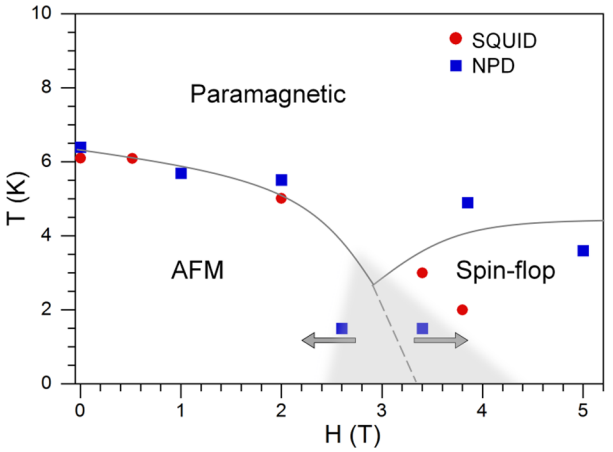

Figure 9. Magnetic phase diagram of Li_2FeGeS_4 mapped using constant-wavelength neutron powder diffraction data and magnetization data obtained using a SQUID magnetometer. Lines provide guides for the eye to approximate magnetic phase boundaries.

observed magnetic moment is lower than the magnetic moment of the free ion. A similar moment of 3.5 μ_B/Fe was obtained for Cu_2FeGeS_4, with a propagation vector $\mathbf{k}_m$ = [$^1/_2$, 0, $^1/_2$], using neutron diffraction.[23]

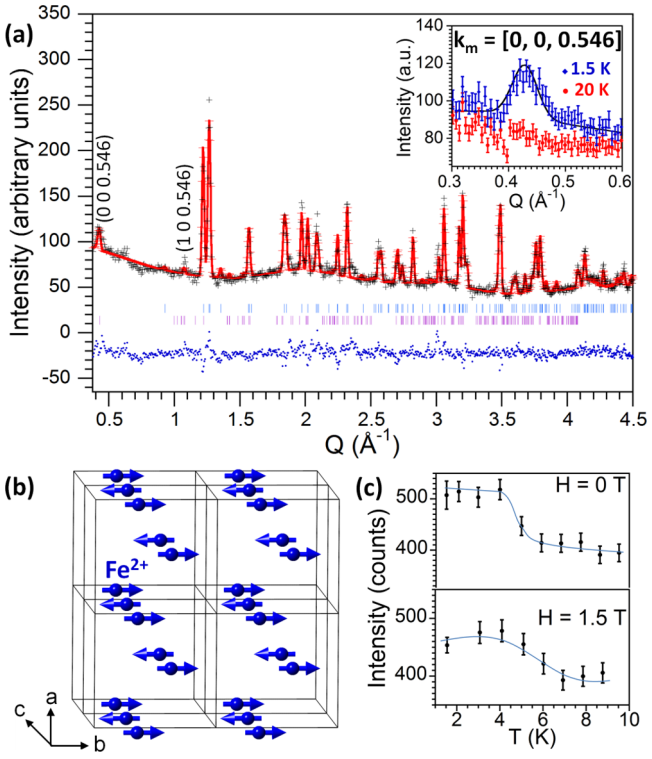

Figure 10. (a) Rietveld refinement of constant-wavelength neutron powder diffraction data for Li_2FeSnS_4 collected at 1.5 K. Indices for main peaks from the magnetic structure are labeled. Bragg reflections for the nuclear and magnetic structures are displayed from top to bottom with tick marks (|). The difference between the collected data (+) and the calculated pattern (line) is shown at the bottom of the plot. The inset shows a peak attributed to magnetic ordering, and the fit of the magnetic structure is shown with a line. (b) Magnetic ordering in Li_2FeSnS_4. (c) Temperature dependence of the intensities of the magnetic peak at 0.43 Å^{-1}. Lines provide guides for the eye.

Just as in LIGS, the magnetic moments in LITS are aligned along the *b* axis, and the moments associated with this AFM ordering get smaller as applied field strength increases. With the collinear model, the metamagnetic phase has a refined magnetic moment of 1.9(4) μ_B/Fe but is statistically difficult to confirm. This model, while physically reasonable, does not necessarily represent a distinct solution since the diffracted intensities from the magnetic phase are low and do not provide sufficient information. The magnetic peak at 0.43 Å^{-1} was followed with varying temperature and applied field to establish boundaries in the magnetic phase diagram (Figure 11). According to the CW-NPD data, the onset of magnetic ordering occurs at ~5.0 K under zero field as well as an applied field of 1.5 T. When the magnetic peak intensity was followed with varying applied field (0 to 3.5 T) at a constant temperature of 1.5 K, the onset of spin-flop occurred at ~1.7 T, and the spin-flop phase became unobservable using NPD at ~3.4 T upon approaching the saturation field. It should be noted that the magnetic ordering likely approaches a ferromagnetic state upon saturation.

In both LIGS and LITS, there are no direct Fe−Fe or Fe−S−Fe pathways. In fact, iron sites are encountered only in the fourth coordination sphere of a given iron site; the pathways are Fe−S−Ge(Sn)−S−Fe and Fe−S−Li−S−Fe. In both structures, iron sites constitute undulating layers that are stacked between S, Li, and Ge or Sn sites. The shortest Fe···Fe distances are 5.508 and 5.576 Å in LIGS and LITS, respectively;

dx.doi.org/10.1021/ic5011693 | *Inorg. Chem.* XXXX, XXX, XXX−XXX

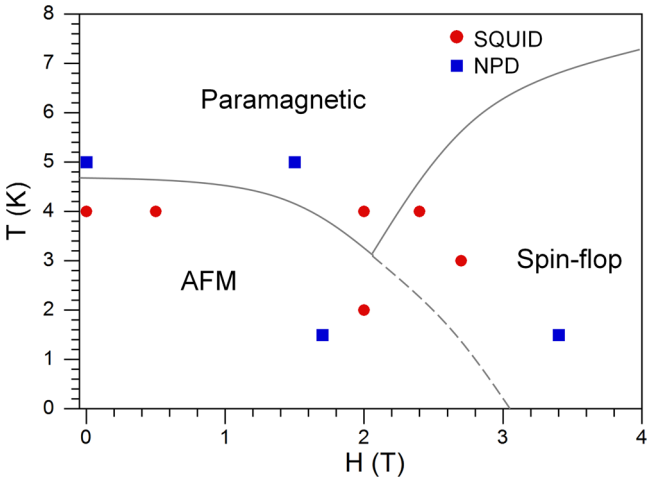

Figure 11. Magnetic phase diagram of Li_2FeSnS_4 mapped using constant-wavelength neutron powder diffraction data and magnetization data obtained using a SQUID magnetometer. Lines provide guides for the eye to distinguish magnetic phases.

thus, the magnetic ordering does not arise from direct iron–iron interactions. Although bound magnetic polarons are responsible for magnetic ordering in similar quaternary DLSs (e.g., $Cu_2FeGeSe_4$),[10e,h,11,14b] they were not observed in the data presented herein.

CONCLUSION

Interestingly, simply altering the tetravalent ion in $Li_2Fe–IV–S_4$ DLSs from Ge to Sn changes the magnetic structure from commensurate to incommensurate. Furthermore, the electronic band structure is significantly varied. An indirect optical bandgap of 1.42 eV is observed for LIGS, while a direct gap of 1.86 eV is observed for LITS. Meanwhile, the wurtz-kesterite structure is preserved, as well as the overall AFM behavior, spin-flop, and general layout of the magnetic phase diagrams.

As $I_2–II–IV–VI_4$ materials are designed to reliably direct divalent ions to specific locations within diamond-like structures, Fe^{2+} ions are ordered and separated within LIGS and LITS DLSs to generate magnetic ordering. This work demonstrates that the bandgaps and magnetic interactions in $I_2–II–IV–VI_4$ DLSs can be delicately tuned. Around 100 magnetic $I_2–II–IV–VI_4$ DLSs can be postulated with I = Li, Cu, or Ag; II = Mn, Fe, Co, or Ni; IV = Si, Ge, or Sn; and VI = S, Se, or Te. Furthermore, nearly countless phases can be accessed through the preparation of solid solutions. Therefore, these materials provide a wide playing field for the future discovery of new magnetic semiconductors. In-depth structural and physicochemical characterizations of quaternary DLSs are warranted in the pursuit of more desirable magnetic properties.

ASSOCIATED CONTENT

Supporting Information

Synchrotron powder diffraction, neutron powder diffraction, Rietveld refinement, Mössbauer spectroscopy, Curie–Wiess fits, and magnetic susceptibility. This material is available free of charge via the Internet at http://pubs.acs.org.

AUTHOR INFORMATION

Corresponding Author

*E-mail: aitkenj@duq.edu.

Notes

The authors declare no competing financial interest.

ACKNOWLEDGMENTS

This work was supported by the National Science Foundation (Grants DMR-1201729 and DMR-0645304). A portion of this research at Oak Ridge National Laboratory's High Flux Isotope Reactor and Spallation Neutron Source was sponsored by the Scientific User Facilities Division, Office of Basic Energy Sciences, U.S. Department of Energy (IPTS-6435, IPTS-8267, and IPTS-10859). Use of the Advanced Photon Source at Argonne National Laboratory was supported by the U.S. Department of Energy, Office of Science, Office of Basic Energy Sciences, under Contract DE-AC02-06CH11357 (GUP-33598). We thank Jason Hodges, Ashfia Huq, and Mike Shatruk for help with data collections and for valuable discussions.

REFERENCES

(1) (a) Dietl, T. *Nat. Mater.* **2003**, *2*, 646–648. (b) Erwin, S. C.; Žutić, I. *Nat. Mater.* **2004**, *3*, 410–414.

(2) (a) Hall, S. R.; Stewart, O. M. *Acta Crystallogr., Sect. B* **1973**, *29*, 579–585. (b) Zhao, Y.-J.; Zunger, A. *Phys. Rev. B* **2004**, *69*, No. 104422.

(3) (a) Picozzi, S.; Zhao, Y.-J.; Freeman, A. J.; Delley, B. *Phys. Rev. B* **2002**, No. 205206. (b) Yao, J.; Brunetta, C. D.; Aitken, J. A. *J. Phys.: Condens. Matter* **2012**, *24*, No. 086006. (c) Yao, J.; Wang, Z.; van Tol, J.; Dalal, N. S.; Aitken, J. A. *Chem. Mater.* **2010**, *22*, 1647–1655. (d) Yao, J.; Kline, C. N.; Gu, H.; Yan, M.; Aitken, J. A. *J. Solid State Chem.* **2009**, *182*, 2579–2586. (e) Yao, J.; Takas, N. J.; Schliefert, M. L.; Paprocki, D. S.; Blanchard, P. E. R.; Gou, H.; Mar, A.; Exstrom, C. L.; Darveau, S. A.; Poudeu, P. F. P.; Aitken, J. A. *Phys. Rev. B* **2011**, *84*, No. 075203.

(4) Dietl, T.; Ohno, H.; Matsukura, F.; Cibert, J.; Ferrand, D. *Science* **2000**, *287*, 1019–1022.

(5) (a) Jungwirth, T.; Sinova, J.; Masek, J.; Kucera, J.; MacDonald, A. H. *Rev. Mod. Phys.* **2006**, *78*, 809–864. (b) Pearton, S. J.; Abernathy, C. R.; Norton, D. P.; Hebard, A. F.; Park, Y. D.; Boatner, L. A.; Budai, J. D. *Mater. Sci. Eng., R* **2003**, *40*, 137–168.

(6) (a) Lekse, J. W.; Leverett, B. M.; Lake, C. H.; Aitken, J. A. *J. Solid State Chem.* **2008**, *181*, 3217–3222. (b) Brunetta, C. D.; Karuppannan, B.; Rosmus, K. A.; Aitken, J. A. *J. Alloys Compd.* **2012**, *516*, 65–72. (c) Rosmus, K. A.; Brunetta, C. D.; Srnec, M. N.; Karuppannan, B.; Aitken, J. A. *Z. Anorg. Allg. Chem.* **2012**, *638*, 2578–2584. (d) Lekse, J. W.; Moreau, M. A.; McNerny, K. L.; Yeon, J.; Halasyamani, P. S.; Aitken, J. A. *Inorg. Chem.* **2009**, *48*, 7516–7518. (e) Brant, J. A.; Clark, D. J.; Kim, Y. S.; Jang, J. I.; Zhang, J.-H.; Aitken, J. A. *Chem. Mater.* **2014**, *26*, 3045–3048.

(7) (a) Parthé, E. *Crystal Chemistry of Tetrahedral Structures*; Gordon and Breach Science Publishers: New York, 1964. (b) Goryunova, N. A. *The Chemistry of Diamond-like Semiconductors*; Massachusetts Institute of Technology: Cambridge, MA, 1965. (c) Pamplin, B. *Prog. Cryst. Growth Charact.* **1981**, *3*, 179–192. (d) Pamplin, B. R. *J. Phys. Chem. Solids* **1964**, *25*, 675–684.

(8) Pauling, L. *J. Am. Chem. Soc.* **1929**, *51*, 1010–1026.

(9) Caneschi, A.; Cipriani, C.; Di Benedetto, F.; Sessoli, R. *Phys. Chem. Miner.* **2004**, *31*, 190–193.

(10) (a) Nénert, G.; Palstra, T. T. M. *J. Phys.: Condens. Matter* **2009**, *21*, No. 176002. (b) Quintero, E.; Quintero, M.; Moreno, E.; Lara, L.; Morocoima, M.; Pineda, F.; Grima, P.; Tovar, R.; Bocaranda, P.; Henao, J. A.; Macías, M. A. *J. Phys. Chem. Solids* **2010**, *71*, 993–998. (c) Rincón, C.; Quintero, M.; Moreno, E.; Power, C.; Quintero, E.; Henao, J. A.; Macías, M. A.; Delgado, G. E.; Tovar, R.; Morocoima, M. *Solid State Commun.* **2011**, *151*, 947–951. (d) Fries, T.; Shapira, Y.; Palacio, F.; Morón, C.; McIntyre, G. J.; Kershaw, R.; Wold, A.; McNiff, E. J. *Phys. Rev. B* **1997**, *56*, 5424–5431. (e) Quintero, M.; Tovar, R.; Barreto, A.; Quintero, E.; Rivero, A.; Gonzalez, J.; Porras, G. S.; Ruiz,

dx.doi.org/10.1021/ic5011693 | *Inorg. Chem.* XXXX, XXX, XXX–XXX

J.; Bocaranda, P.; Broto, J. M.; Rakoto, H.; Barbaste, R. *Phys. Status Solidi B* **1998**, *209*, 135−143. (f) Bernardini, G. P.; Borrini, D.; Caneschi, A.; Di Benedetto, F.; Gatteschi, D.; Ristori, S.; Romanelli, M. *Phys. Chem. Miner.* **2000**, *27*, 453−461. (g) Allemand, J.; Wintenberger, M. *Bull. Soc. Fr. Mineral. Crystallogr.* **1970**, *93*, 14−17. (h) Quintero, E.; Quintero, M.; Morocoima, M.; Bocaranda, P. *J. Appl. Phys.* **2007**, *102*, No. 083905.

(11) Quintero, E.; Tovar, R.; Quintero, M.; Gonzalez, J.; Broto, J. M.; Rakoto, H.; Barbaste, R.; Woolley, J. C.; Lamarche, G.; Lamarche, A.-M. *J. Magn. Magn. Mater.* **2000**, *210*, 208−214.

(12) Woolley, J. C.; Lamarche, G.; Lamarche, A.-M.; Rakoto, H.; Broto, J. M.; Quintero, M.; Morocoima, M.; Quintero, E.; Gonzalez, J.; Tovar, R.; Cadenas, R.; Bocoranda, P.; Ruiz, J. *J. Magn. Magn. Mater.* **2003**, *257*, 87−94.

(13) Chen, X. L.; Lamarche, A.-M.; Lamarche, G.; Woolley, J. C. *J. Phys.: Condens. Matter* **1993**, *5*, 7143−7154.

(14) (a) Quintero, E.; Quintero, M.; Moreno, E.; Morocoima, M.; Grima, P.; Bocaranda, P.; Henao, J. A.; Pinilla, J. *J. Alloys Compd.* **2009**, *471*, 16−20. (b) McCabe, G. H.; Fries, T.; Liu, M. T.; Shapira, Y. *Phys. Rev. B* **1997**, *56*, 6673−6680.

(15) (a) Wang, J.; Toby, B. H.; Lee, P. L.; Ribaud, L.; Antao, S.; Kurtz, C.; Ramanathan, M.; Von Dreele, R. B.; Beno, M. A. *Rev. Sci. Instrum.* **2008**, *79*, No. 085105. (b) Lee, P. L.; Shu, D.; Ramanathan, M.; Preissner, C.; Wang, J.; Beno, M. A.; Von Dreele, R. B.; Ribaud, L.; Kurtz, C.; Antao, S. M.; Jiao, X.; Toby, B. H. *J. Synchrotron Radiat.* **2008**, *15*, 427−432. (c) Dalesio, L. R.; Hill, J. O.; Kraimer, M.; Lewis, S.; Murray, D.; Hunt, S.; Watson, W.; Clausen, M.; Dalesio, J. *Nucl. Instrum. Methods Phys. Res., Sect. A* **1994**, *352*, 179−184.

(16) (a) Larson, A. C.; Von Dreele, R. B. *General Structure Analysis System (GSAS)*; Los Alamos National Laboratory Report LAUR 86-748, 1994. (b) Toby, B. H. *J. Appl. Crystallogr.* **2001**, *34*, 210−213.

(17) Huq, A.; Hodges, J. P.; Gourdon, O.; Heroux, L. *Z. Kristallogr. Proc.* **2011**, *1*, 127−135.

(18) Carvajal-Rodríguez, J. *Physica B* **1993**, *192*, 55−69.

(19) Douvalis, A. P.; Polymeros, A.; Bakas, T. *J. Phys. Conf. Ser.* **2010**, *217*, No. 012014.

(20) Kubelka, P.; Munk, F. *Z. Technol. Phys.* **1931**, *12*, 593−601.

(21) (a) Urbach, F. *Phys. Rev.* **1953**, *92*, 1324. (b) Pankove, J. I. *Optical Properties in Semiconductors*; Dover Publications: New York, 1971.

(22) Bain, G. A.; Berry, J. F. *J. Chem. Educ.* **2008**, *85*, 532−536.

(23) Wintenberger, M. *Mater. Res. Bull.* **1979**, *14*, 1195−1202.

(24) Brockway, L. O. *Z. Kristallogr., Kristallgeom., Kristallphys. Kristallchem.* **1934**, *89*, 434−441.

(25) Bundy, F. P.; Kasper, J. S. *J. Chem. Phys.* **1967**, *46*, 3437−3446.

(26) (a) Brunetta, C. D.; Brant, J. A.; Rosmus, K. A.; Henline, K. M.; Karey, E.; MacNeil, J. H.; Aitken, J. A. *J. Alloys Compd.* **2013**, *574*, 495−503. (b) Ilyukhin, V. V.; Nikitin, A. V.; Belov, N. V. *Sov. Phys. Dokl. (Engl. Transl.)* **1966**, *11*, 1035−1038. (c) Parthé, E.; Yvon, K.; Deitch, R. H. *Acta Crystallogr.* **1969**, *25*, 1164−1174.

(27) Lafond, A.; Choubrac, L.; Guillot-Deudon, C.; Fertey, P.; Evain, M.; Jobic, S. *Acta Crystallogr., Sect. B* **2014**, *70*, 390−394.

(28) (a) Siebentritt, S.; Schorr, S. *Prog. Photovoltaics* **2012**, *20*, 512−519. (b) Schorr, S. *Sol. Energy Mater. Sol. Cells* **2011**, *95*, 1482−1488.

(29) Shannon, R. D. *Acta Crystallogr.* **1976**, *32*, 751−767.

(30) (a) Di Benedetto, F.; Bernardini, G. P.; Borrini, D.; Lottermoser, W.; Tippelt, G.; Amthauer, G. *Phys. Chem. Miner.* **2005**, *31*, 683−690. (b) Eibschütz, M.; Hermon, E.; Shtrikman, S. *J. Phys. Chem. Solids* **1967**, *28*, 1633−1636. (c) Marfunin, A. S.; Mkrtchyan, A. R. *Geokhimiya* **1967**, *10*, 1094−1103. (d) Vaughan, D. J.; Burns, R. G. *Proc. Int. Geol. Congr., 24th,* **1972**, 158−167. (e) Yamanaka, T.; Kato, A. *Am. Mineral.* **1976**, 260−265. (f) Baldini, A.; Bernardini, G. P.; Cianchi, L.; Gulisano, F.; Manchini, M.; Spina, G. *Hyperfine Interact.* **1989**, *46*, 695−699.

(31) Mackovicky, E.; Forcher, K.; Lottermoser, W.; Amthauer, G. *Mineral. Petrol.* **1990**, *43*, 73−81.

(32) (a) Hu, J.; Lu, Q.; Deng, B.; Tang, K.; Qian, Y.; Li, Y.; Zhou, G.; Liu, X. *Inorg. Chem. Commun.* **1999**, *2*, 569−571. (b) Wang, M. X.; Wang, L. S.; Yue, G. H.; Wang, X.; Yan, P. X.; Peng, D. L. *Mater. Chem. Phys.* **2009**, *115*, 147−150.

(33) (a) Burnett, J. D.; Xu, T.; Sorescu, M.; Strohmeier, B. R.; Sturgeon, J.; Gourdon, O.; Baroudi, D.; Yao, J.-L.; Aitken, J. A. *J. Solid State Chem.* **2013**, *197*, 279−287. (b) Forcher, K.; Lottermoser, W.; Amthauer, G. *Neues Jahrb. Mineral., Abh.* **1988**, *160*, 25−28.

(34) Nord, A. G.; Ericsson, T. *Am. Mineral.* **1982**, *67*, 826−832.

(35) (a) Shinno, I.; Li, Z. *Am. Mineral.* **1998**, *83*, 1316−1322. (b) Ericsson, T.; Nord, A. G. *Am. Mineral.* **1984**, *69*, 889−895. (c) Mattievich, E.; Danon, J. *J. Inorg. Nucl. Chem.* **1977**, *39*, 569−580. (d) Moore, P. B.; Araki, T. *Am. Mineral.* **1973**, *58*, 302−307. (e) Mori, H.; Ito, T. *Acta Crystallogr.* **1950**, *3*, 1−6. (f) Nomura, K.; Ujihira, Y. *Nippon Kagaku Kaishi* **1982**, 1352−1356.

(36) (a) Greatrex, R.; Greenwood, N. N.; Ribes, M. *J. Chem. Soc., Dalton Trans.* **1976**, 500−504. (b) Ibanez, A.; Jumas, J. C.; Philippot, E.; Ajavon, A. L.; Eholie, R. *Rev. Chim. Miner.* **1986**, *23*, 281−289.

(37) (a) Ichiba, S.; Katada, M.; Negita, H. *Chem. Lett.* **1974**, 979−982. (b) Amthauer, G.; Fenner, J.; Hafner, S.; Holzapfel, W. B.; Keller, R. *J. Chem. Phys.* **1970**, *70*, 4837−4842.

(38) Stevens, J. G.; Goforth, M. A.. *^{119}Sn Mössbauer Spectroscopy*; Mössbauer Effect Data Center: Asheville, NC, 1993.

(39) (a) Ledda, F.; Muntoni, C.; Serci, S. *Chem. Phys. Lett.* **1987**, *134*, 545−548. (b) von Feltz, A.; Schlenzig, E.; Arnold, D. *Z. Anorg. Allg. Chem.* **1974**, *403*, 243−250.

(40) (a) Donaldson, J. D.; Senior, B. J. *J. Inorg. Nucl. Chem.* **1969**, *31*, 881−884. (b) Greenwood, N. N.; Gibb, T. C. *Mossbauer Spectroscopy*; Chapman and Hall: London, 1971.

(41) del Bucchia, S.; Jumas, J. C.; Maurin, M. *Acta Crystallogr., Sect. B* **1981**, *37*, 1903−1905.

(42) (a) Baur, W. H. *Acta Crystallogr.* **1956**, *9*, 515−520. (b) Izumi, F. *J. Solid State Chem.* **1981**, *38*, 381−385.

(43) Tauc, J. *MRS Bull.* **1968**, *3*, 37−46.

(44) (a) Chen, S.; Walsh, A.; Luo, Y.; Yang, J.-H.; Gong, X. G.; Wei, S.-H. *Phys. Rev. B* **2010**, *82*, No. 195203. (b) Goetzberger, A.; Hebling, C.; Schock, H.-W. *Mater. Sci. Eng., R* **2003**, *40*, 1−46.

(45) (a) Anderson, F. B.; Callen, H. B. *Phys. Rev.* **1964**, *136*, A1068−A1086. (b) Keffer, F.; Chow, H. *Phys. Rev. Lett.* **1973**, *31*, 1061−1063.

(46) (a) Guen, L.; Glaunsinger, W. S. *J. Solid State Chem.* **1980**, *35*, 10−21. (b) Ganiel, U.; Herman, E.; Shtrikman, S. *J. Phys. Chem. Solids* **1972**, *33*, 1873−1878.